AIAA JOURNAL
Vol. 39, No. 6, June 2001

Insights in Turbulence Modeling for Crossing-Shock-Wave/Boundary-Layer Interactions

Frédéric Thivet*
ONERA, 31055 Toulouse Cedex 4, France
Doyle D. Knight†
Rutgers University, Piscataway, New Jersey 08854
and
Alexander A. Zheltovodov‡ and Alexander I. Maksimov§
Institute of Theoretical and Applied Mechanics, Novosibirsk, 630090, Russia

The impact of turbulence modeling on the numerical simulation of the crossing-shock-wave/boundary-layer interactions occuring in a Mach 4 flow on 7 × 7 deg, 7 × 11 deg, and 15 × 15 deg double-sharp fin plates is analyzed. The full Reynolds-averaged Navier–Stokes equations are solved with linear and weakly nonlinear formulations of the k–ω turbulence model, on grids up to 4×10^6 cells. The overpredicted heat transfer on the bottom plate is shown to be closely related to the main three-dimensional features developing in these flows. The stronger the interaction, the more the numerical solutions violate the realizability principles. By introducing a dependence of c_θ on the velocity gradients, realizable solutions are obtained and analyzed. The heat-transfer coefficients are effectively lowered but not sufficiently to meet the experimental data. The expected impact of other corrections, based on a limitation of the turbulent length scale or some compressibility effects, is evaluated and shown to be insufficient to fill the gap between computed and measured heat-transfer coefficients. The streamlines arriving near the wall in the regions of overpredicted heat transfer are shown to originate from the very narrow regions close to the fin leading edges, in the upper part of the incoming boundary layer, and to be associated with an increase of turbulent kinetic energy when approaching the bottom wall, rather than when crossing the shock waves.

Nomenclature

C_h	=	heat-transfer coefficient or Stanton number; Eq. (1)
c_μ	=	coefficient in the constitutive equation for μ_t, 0.09
$D_t(\rho\varphi)$	=	substantial derivative, $\partial\rho\varphi/\partial t + \partial\rho U_i\varphi/\partial X_i$
k	=	turbulent kinetic energy (TKE), $\frac{1}{2}\widetilde{u_i u_i}$
P_k	=	TKE production rate, $-\rho\widetilde{u_i u_j} S_{ij}$
S	=	strain invariant, $\sqrt{(2S^\circ_{ij} S^\circ_{ij})}$
S_{ij}	=	strain rate, $\frac{1}{2}(\partial U_i/\partial x_j + \partial U_j/\partial x_i)$
S°_{ij}	=	traceless strain rate, $S_{ij} - \frac{1}{3}S_{kk}\delta_{ij}$
s	=	dimensionless strain invariant, S/ω
U_i	=	mass-averaged velocity components U, V, W
u_i	=	fluctuating velocity components u, v, w (mass averaging)
$\widetilde{u_i u_j}$	=	mass-averaged velocity correlations
x_j	=	Cartesian coordinates x, y, z
α_v	=	realizability factor; Eq. (8)
δ_{ij}	=	Kronecker symbol
δ_0	=	incoming boundary-layer thickness, 3.5 mm
ϵ	=	dissipation of TKE
μ, ν	=	dynamic and kinematic molecular viscosities, $\mu = \rho\nu$
μ_t, ν_t	=	Dynamic and kinematic turbulent viscosities, $\mu_t = \rho\nu_t$
ϖ	=	dimensionless vorticity invariant, Ω/ω
ρ	=	mass density
Ω	=	vorticity invariant, $\sqrt{(2\Omega_{ij}\Omega_{ij})}$
Ω_{ij}	=	vorticity, $\frac{1}{2}(\partial U_i/\partial x_j - \partial U_j/\partial x_i)$
ω	=	specific dissipation of TKE, ϵ/k

Received 29 May 2000; revision received 9 October 2000; accepted for publication 13 October 2000.

*Senior Research Engineer, Department of Models for Aerodynamics and Energetics, Centre de Toulouse. Member AIAA.
†Professor of Aerospace and Mechanical Engineering, Department of Mechanical and Aerospace Engineering. Associate Fellow AIAA.
‡Senior Research Scientist and Chief, Separated Flows Research Group. Senior Member AIAA.
§Senior Research Scientist, Separated Flows Research Group.

Introduction

UNDERSTANDING and modeling crossing-shock-wave/turbulent boundary-layer interactions (CSWBLI) is of critical importance for predicting the performance of supersonic inlets. The complex three-dimensional interactions occurring in supersonic inlets are accurately reproduced in very simple geometrical configurations, namely the single- and double-sharp fin plate: one or two fins with sharp leading edge are mounted on a flat plate with different combinations of deflection angles (Fig. 1). In the past 15 years numerous experimental and computational studies have been carried out on these configurations. In a 1993 AGARD report,[1] Settles[2] provided a thorough review of the features of the flow on single-sharp fin plates. A series of investigators have identified the main features of the flows on double-sharp fin plates. Garrison and Settles provided detailed flow visualizations using a planar laser scattering method[3] and proposed a thorough analysis of the shock structures.[4] This first model was then refined and compared with computational results in the 15 × 15 deg Mach 4 configuration. The comparison includes the structure of the shocks,[5] the skin-friction coefficients,[6] the pitot and stagnation pressures, as well as the flow deviations.[7] In parallel Gaitonde et al. provided a first analysis of the main three-dimensional features of these flows, first in a 15 × 15 deg Mach 8.3 configuration[8] and then in the 15 × 15 deg Mach 4 case.[9] These results as well as past[10] and recent[11,12] reviews by Knight and Degrez emphasize the fact that, in a strong SWBLI, the skin-friction and heat-transfer coefficients are generally overestimated by numerical simulations. In the case of the heat transfer, the error can be as large as 100%.

New experiments were conducted by Zheltovodov et al.,[13–15] who provided surface flow visualizations, and surface pressure, adiabatic temperature and heat-transfer coefficient measurements. The capacity of the computations to reproduce the flow features in asymmetric configurations was first assessed by Knight et al.[16] It was evidenced again that the primary flow features (primary separation and attachment lines, global pressure distribution) are not dependent on the

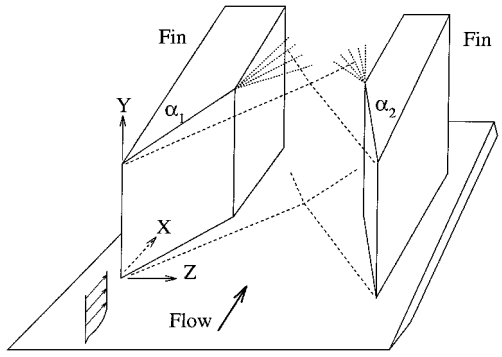

Fig. 1 Double-sharp fin plate configuration.

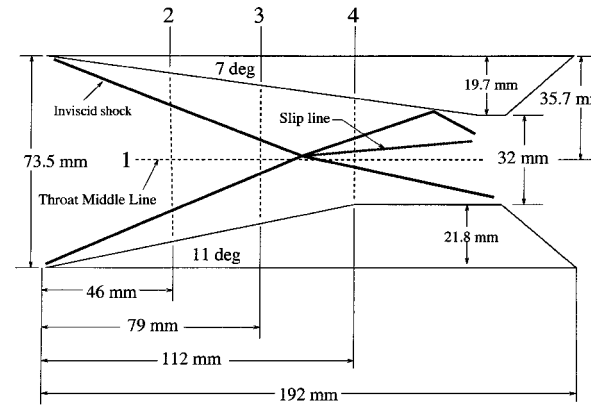

Fig. 2 The 7 × 11 deg experimental model (from Ref. 16).

turbulence model but that the secondary flow features (secondary singular lines, local pressure distribution) and the heat-transfer coefficient are. Gaitonde et al. described the evolution of the flow model with the interaction strength and asymmetry.[17]

From a modeling point of view, recent progress is a result of Panaras,[18,19] who showed that a better prediction of the secondary separated flow could be obtained in the case of single-sharp fin plate by modifying the Baldwin–Lomax[20] algebraic turbulence model. With the same modification some improvement was obtained in the prediction of the pressure and skin-friction distributions in the central separated region of the 15 × 15 deg Mach 4 configuration.[18] A first attempt was made in Ref. 21 to inhibit the transition of the sidewall boundary layer by limiting the production of turbulent kinetic energy in a k–ϵ model; it resulted in a rectification of the discrepancies between the flowfield visualizations and simulations in the sidewall/shock-vortex interaction region but no significant effect on the bottom wall.

This paper addresses the issue of the overprediction of the skin-friction and heat-transfer coefficients in RANS simulations of CSWBLI with two-equation turbulence models. A broad range of conditions is covered by the three selected configurations. A special effort is made to assess the mesh convergence of the computed results. A description of the main features of the flow is provided. It supplements previous descriptions and focuses on the relationship between the three-dimensional features of the flow and the skin-friction lines pattern and Stanton number on the bottom plate. The considered configurations are characterized by high strain rate regions and high-speed flows. First, different realizability corrections are considered to solve the problem encountered by two-equation turbulence models in high strain rate flows. Second, the effect of usual corrections for high-speed flows is assessed. The study concludes on the ability of these corrections in solving the heat-transfer issue in CSWBLI.

Experiments

Experiments were conducted by Zheltovodov et al.[13–15] in the supersonic wind tunnel T-333 (Ref. 22) of the Institute of Theoretical and Applied Mechanics, Novosibirsk, Russia. The model (Fig. 2) is a plate with two mounted fins with sharp leading edges located at 210 mm from the plate leading edge. Chamfered fins are 192 mm long and 100 mm high; they are separated by a minimum distance of 32 mm in the constant-width section (the throat). The x axis is taken at the throat middle line (TML). The six possible pairs of 7-, 11-, and 15-deg wedges have been experimentally studied. The flow Mach number ranges between 3.89 and 3.96, the total pressure between 1480 and 1498 kPa, and the total temperature between 256 and 264 K, yielding a unit Reynolds number between 85.0×10^6 m^{-1} and 93.3×10^6 m^{-1}. On the bottom and side walls surface flow visualizations were obtained using a 10–15% mixture of lampblack and oil. Along the TML and three cross sections ($x = 46$, 79, and 112 mm) the surface pressure, adiabatic temperature, and heat fluxes (in slightly heated wall conditions) were directly measured; the last two quantities were combined to build the heat-transfer coefficient using the electric-calorimetry method with a ±15% accuracy.[14,15,23] The boundary-layer height is $\delta_0 = 3.5$ mm and the momentum thickness 0.128 mm, 14 mm ahead of the fin leading edges.

Numerical Method

Flow Solver and Boundary Conditions

The computations are performed with the code GASPex,[24] which solves the Reynolds-averaged three-dimensional compressible time dependent Navier–Stokes equations (RANS). The convective fluxes are computed to third-order accuracy with the Roe scheme and the MUSCL reconstruction method for the primitive variables with the min-mod limiter. The Sutherland law is used to calculate the laminar viscosity, and a constant laminar Prandtl number of 0.72 is assumed. Central differencing is used to evaluate the viscous terms. The steady solution is obtained by applying a time-marching method based on the hybrid approximate factorization/relaxation algorithm.[24] The first solutions presented here are computed with the k–ω turbulence model by Wilcox[25] and a constant turbulent Prandtl number of 0.9. The slightly rough wall condition is used for the turbulent kinetic energy (TKE) specific dissipation: $\omega_w = N \nu_w / k_s^2$ with $N = 2500$, and the value $k_s^+ = 5$ is chosen to obtain the hydraulically smooth wall solution.[25,26] [Hereafter, the superscript + denotes lengths in wall units: $k_s^+ = k_s \sqrt{(\tau_w / \rho_w)} / \nu_w$, where τ_w is the norm of the wall shear-stress.]

The freestream flow is characterized by a Mach number of 3.92, a total pressure of 1485 kPa, a total temperature of 260 K yielding a unit Reynolds number of 87.48×10^6 m^{-1}. The inflow condition is prescribed after the computation of the boundary layer developing on a 200-mm-long flat plate, carried out with the RANS solver on a very fine mesh: about 400 cells are distributed inside the boundary layer normally to the wall with a first cell height below 0.25 wall unit on 80% of the plate length. The solution is mesh converged to at least 0.1% for the skin-friction and heat-transfer coefficients.[27] Both the isothermal and adiabatic wall conditions are computed. The boundary-layer profiles corresponding to the measured momentum thickness serve as inflow conditions to the three-dimensional computations.

At the top as well as at the outflow boundary, the solution is extrapolated to first order from interior. In the symmetrical cases only half a configuration is computed, and a second-order symmetrical condition is prescribed on the symmetry plane. On the bottom and side walls fully turbulent boundary layers are computed, using either a no-slip adiabatic or isothermal condition. Both sets of results are needed to obtain the heat-transfer coefficient in a manner similar to the one used in the experiments. The adiabatic wall solution provides the adiabatic wall temperature T_{aw}, which ranges between 240–260 K, and the isothermal wall solution provides the heat flux Q_w corresponding to the constant wall temperature $T_{\mathrm{w}} = 270$ K; the heat-transfer coefficient, or Stanton number, is then obtained as

$$C_h = Q_w / \rho_\infty U_\infty C_p (T_w - T_{\mathrm{aw}}) \tag{1}$$

where ρ_∞, U_∞, and C_p are respectively the freestream density, velocity, and heat capacity of air at constant pressure.

Computed Cases and Grids

Of the six configurations experimentally studied at Mach 4, three have been selected for the computations. They cover an interesting range of conditions, including a weak interaction (7 × 7 deg case),

Table 1 Grid parameters

	7 × 7 deg configuration			7 × 11 deg configuration			15 × 15 deg configuration			
Grid	Fine	Medium	Coarse	Fine	Medium	Coarse	Very fine	Fine	Medium	Coarse
N_{cell}	614,400	153,600	38,400	1,228,800	307,200	76,800	3,993,600	998,400	249,600	62,400
$N_y \times N_z$	80 × 80	40 × 40	20 × 20	80 × 160	40 × 80	20 × 40	200 × 104	100 × 104	50 × 52	25 × 26
$N_x / \Delta x$, mm	96/2	96/2	96/2	96/2	96/2	96/2	192/1	96/2	96/2	96/2
Δy_1, μm	1.00	2.15	5.02	1.00	2.15	5.02	0.50	1.02	2.14	4.72
Δy_1^+	0.35–0.5	0.75–1.2	1.9–3.5	0.35–1.3	0.75–3.0	1.9–7.0	0.17–1.0	0.35–2.0	0.75–4.0	1.6–8.2
Δz_1, μm	2.8	5.7	12.5	2.8	5.7	12.5	2.8	2.8	5.7	12.5
Δz_{TML}, mm	0.60	1.30	2.70	0.60	1.30	2.70	0.19	0.19	0.41	0.83

a mild asymmetrical interaction (7 × 11 deg case), and a strong interaction (15 × 15 deg case). In each case, three levels of grid refinement are defined. At each level the longitudinal step size Δx is constant and equal to 2 mm (about 0.6 δ_0). The cells of the fine grid (level 1) are merged two by two in both y and z directions to define the medium grid (level 2). The coarse grid (level 3) is obtained the same way from the medium grid. In the 15 × 15 deg configuration only, a fourth refinement level is defined, namely the very fine grid (level 0), obtained by dividing the cells of the fine grid in two in both the x and y directions. The number of cells in each direction N_x, N_y, N_z; the total number of cells N_{cell}; and the other parameters of the grids are gathered in Table 1 and further described in the following.

The three-dimensional computational domain begins 14 mm ahead of the fins and ends 192 mm downstream. The divergent part of the model is present in the 7 × 11 deg and 15 × 15 deg configurations. Although the experimental models are 100 mm high, the computational domain is limited to 80 mm because no significant gradient in the y direction is visible in the experiment between 70 and 90 mm in the cases under consideration. In the 7 × 7 deg and 7 × 11 deg fine grids the first cell height Δ_{y1} is 1 μm, corresponding to 0.35 wall unit in the incoming boundary layer, and 44 cells are distributed according to a geometrical law between the bottom wall and the incoming boundary-layer thickness δ_0; the other 36 cells are distributed following a second geometrical law from this point to the total height of the computational domain. In the 15 × 15 deg configuration the very fine grid is built following the same principles, using a total of 200 cells in the normal direction y. The first geometrical distribution is composed of 160 cells between the bottom wall and a height of 16 mm (4.6 δ_0), starting from a first cell height of 0.5 μm (0.17 wall unit in the incoming boundary layer).

The domain of interest of the flow is the central part of the throat, after the crossing of the primary shock waves. The side wall boundary layers may have an influence on the central region only after the reflection of the shock waves on the fins, i.e., far after the zone of interest. For this reason the mesh cell width off one fin is not as fine as on the bottom wall: Δ_{z1} is prescribed at 2.8 μm in the fine grids, which corresponds to 1.5–3 wall units for the side-wall boundary layer (before the interaction with the reflected shock). Because the first shock/shock interaction occurs at or near the TML, it is chosen to control the cell width in this region also: the first cell off the TML has a constant width $\Delta_{z_{\text{TML}}}$ of 0.6 mm (0.19 mm in the 15 × 15 deg case). A double geometrical law is calculated to match these constraints.

Computational Resources and Strategy

The computations were carried out at the National Center for Supercomputing Applications, University of Illinois at Urbana–Champaign. The code was run in parallel on 32 to 128-thread SGI Cray Origin2000 computers based on 195MHz–390 Mflops R10000 processors by automatically splitting the computational domain into the same number of zones. A Courant–Friedrichs–Lewy (CFL) number of 0.2 was kept in most cases, and the time step was computed locally. The computation on one refinement level was stopped when the maximum value of the residuals was under 10^{-6} for the conservative variables, which means that the relative convergence error was under 10^{-4} for the wall coefficients.[27] The level-n solution was initialized from the level-$(n+1)$ solution. Typically, the computation on the fine-grid solution in the mild or strong interaction case requires 1500 computational hours (about 12 hours on 128 threads).

Flow Analysis

In the three configurations the solutions are successively obtained on the coarse, medium, and fine grids with the Wilcox's k–ω turbulence model and the no-slip, adiabatic wall condition. Nine other solutions were also obtained with the no-slip, isothermal wall condition. (The finest 10th grid is reserved for computations with another model; see the following.)

Mesh Convergence

The mesh convergence is verified for the pressure, adiabatic temperature, skin-friction, and heat-transfer coefficients in the interaction region on the bottom wall. A precise evaluation is performed for the pressure p and heat-transfer coefficient C_h using the mesh-convergence index. For instance, the pressure fine-grid index is the rms of the relative difference in pressure on the bottom wall S_B between the fine and the medium grids:

$$\text{Ind}(p) = \sqrt{\left\{ \int_{S_B} \left[\frac{P_2(x,0,z)}{P_1(x,0,z)} - 1 \right]^2 \mathrm{d}S \right\} \Big/ \left\{ \int_{S_B} \mathrm{d}S \right\}} \qquad (2)$$

where P_1 and P_2 are the pressure fields obtained on the fine and medium grids, respectively. The summation is discretized on the coarsest of the two grids and is limited to the region of the bottom wall between $x = 50 - 130$ mm: the upstream part is removed to eliminate the incoming boundary layer (where the fine-grid indices are below 1 and 1.5% for p and C_h respectively), and the downstream part is removed to focus on the interaction region itself.

In the 7 × 7 deg case the pressure and C_h fine-grid indices are respectively below 2 and 4%, which ensures that the fine-grid solution is mesh converged in the zone of interest (Fig. 3a, bottom curves). For $x > 130$ mm the indices remain below 4 and 9%, respectively. In the 7 × 11 deg case, the pressure and C_h fine-grid indices are respectively below 5.5 and 10%. Considering that the indices are 9.5 and 40% between the medium and coarse grids and examining the solutions along the TML (Fig. 3b) and three cross sections (not shown), it is concluded that the fine-grid solution is very close to the mesh-converged solution. This is confirmed by a local refinement study in x, y, and z in the region of the 11-deg fin leading edge. In the 15 × 15 deg case the pressure and C_h fine-grid indices are respectively 15 and 23%. A refined grid in both x and y is available, but the cost of one computation is so high that only two were affordable. The choice was to do these computations with a modified model (see the following); the pressure and C_h indices are respectively 6 and 10% between the fine and very fine grids with the modified model. In the 15 × 15 deg configuration as well as in the other ones, the solution obtained on the fine grid may be compared with confidence with experimental data.

The heat-transfer coefficient obtained on the coarse grid in the 15 × 15 deg case compares very well to the experimental data (Fig. 3a). Of course, this occurs only by chance and has no particular meaning. It is nevertheless interesting as an illustration of how wrong conclusions can be drawn from solutions that are not mesh converged.

Heat-Transfer Issue

Because similar results have already been extensively commented in the literature,[10,11] only the plots of the heat-transfer coefficient C_h

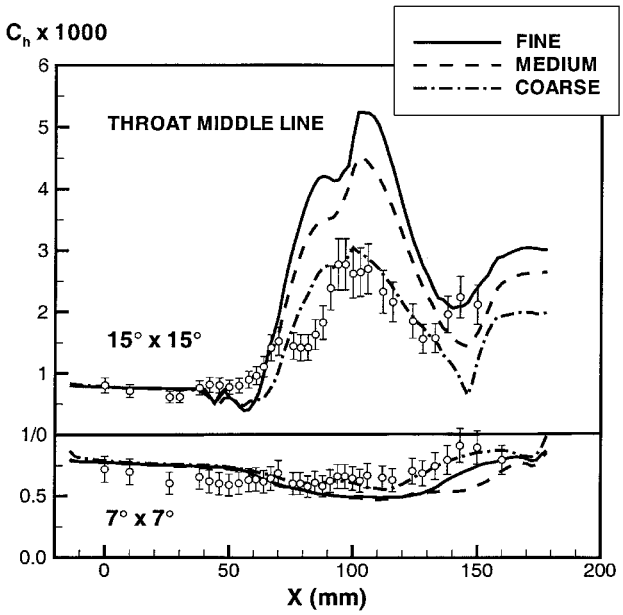

a) Heat-transfer coefficient: 7 × 7 and 15 × 15 deg

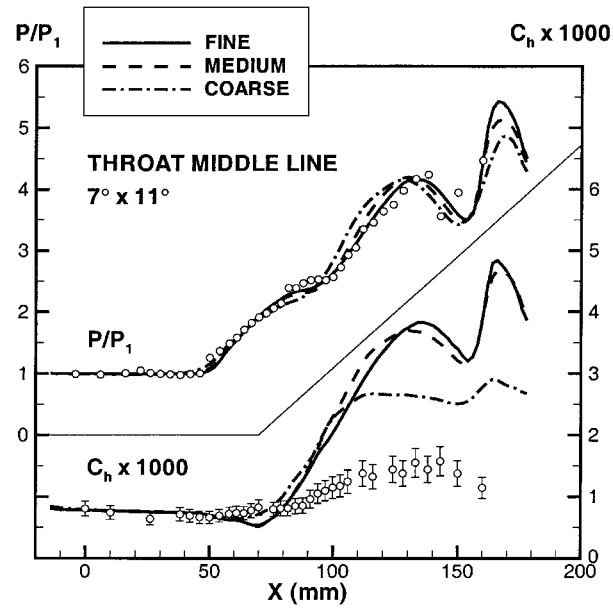

b) Pressure and heat-transfer coefficient: 7 × 11 deg

Fig. 3 Distributions along the TML: Wilcox model.

along the TML are given here (Fig. 3); a comprehensive comparison between present computations and experimental data is presented in Ref. 28. In the incoming boundary layer the computed C_h agrees with experiment to within the experimental uncertainty. In the 7 × 7 deg configuration the simulation predicts the same features as in the experiment: a downward slope of C_h after the primary shock waves have reached the TML, followed by a mild increase further downstream. The level of C_h is somewhat underestimated with respect to the measurements. In the 7 × 11 deg and 15 × 15 deg configurations the first downward slope is also present, but much shorter, and followed by a large increase, up to 2.5 times above the experimental data. At some point (7 × 11 deg: $x = 135$ mm, 15 × 15 deg: $x = 85$ mm) the heat-transfer coefficient pauses and drops a little before rising up to a second maximum, even larger than the first one. In the 15 × 15 deg configuration C_h then drops down and experiences another increase in the divergent part of the device. These features are common to all two-equation turbulence models that have been tested in similar (if not identical) situations.[10,11] The trends are the same for the skin-friction coefficient, which becomes negative on a short length along the TML in the 15 × 15 deg configuration only. To clarify the relation between the skin-friction and heat-flux peaks on the bottom wall and the overall structure of the flows, further analysis is needed.

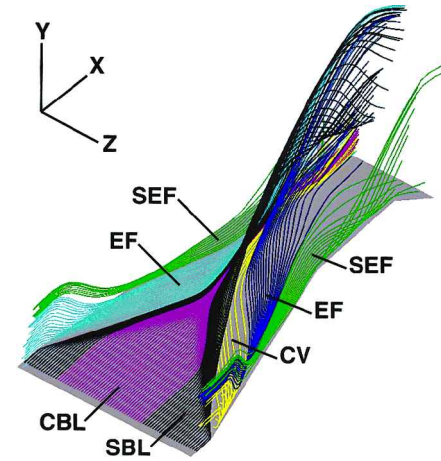

Fig. 4 The 7 × 11 deg, Wilcox model. Streamlines illustrating the different regimes of the flow: 1-black, separated boundary layer (SBL); 1c-purple, centerline boundary layer (CBL); 3-yellow, centerline vortex (CV); 4-blue, entrainment flow, 11-deg fin side (EF); 4-cyan, entrainment flow, 7-deg fin side (EF); and 4s-green, side entrainment flow (SEF).

Flow Regimes and Heat-Flux Peaks

As pointed out by Gaitonde and Shang,[8,9] different coherent features, or regimes, can be identified in the flow. The analysis is completed here, using a somewhat different visualization technique, to show how closely the regimes are related to the shear-stress and Stanton-number distributions on the bottom plate. The regimes are present with some variations in both the 7 × 11 deg and 15 × 15 deg configurations, but only the first one is used here for the illustration (see Refs. 28 and 29 for the second one as well). In Fig. 4 the bottom plate is represented in gray in its full length of 192 mm. The side walls are not displayed for clarity. The width of the device is 73.6 mm at the entrance. A magnification factor of 10 is used in the direction normal to the bottom plate. The green streamlines starting points are about 2.5 mm above the bottom plate ($\sim 0.7\delta_0$). The maximum height reached by the black and cyan streamlines is about 6.5 mm ($\sim 1.85\delta_0$). Four main coherent features may be identified. Selected streamlines are displayed and colored after their respective flow regime. Because the streamlines are displayed only if starting from or reaching the wall region (between 10 and 50 μm, i.e., 0.003 and $0.014\delta_0$), their envelope can be viewed as part of the boundary of the coherent features.

The first regime is the separated boundary layer (SBL) represented by the black lines in Fig. 4. The footprint of this primary separation is the pair of convergence lines visible in the computation as well as in the experiment (S_1 and S_2 in Fig. 5). The only difference between both is that the computed separation lines merge while they remain distinct in the experiment. Along these lines the computations show that the wall heat fluxes (Fig. 5) and skin friction are notably lowered. Some central part of the incoming boundary layer, close to the wall, does not separate when crossing the residual shock waves generated by the fins (Fig. 4, regime 1c in purple); the streamlines first converge toward the meeting point of the primary shock waves, then manage to go through and to remain very close to the wall until the end of the configuration. In stronger interactions, like the 15 × 15 deg case for instance, the whole incoming boundary layer separates, and this subregime disappears. This is why it is not mentioned in previous analyses.[8,9,17] The second regime, namely the vortex interaction flow (VI), is constituted by fluid separating from the downstream side of the primary separation lines. It is present on the 11-deg fin side (but not displayed), and very hardly distinguishable on the 7-deg fin side, as previously noted in asymmetrical configurations.[17]

The region below SBL and VI is occupied by a helical-type flow originating from the upper part of the boundary layer and the inviscid region above; the corresponding envelope streamlines, displayed in blue (11-deg side) and cyan (7-deg side) in Fig. 4, cross

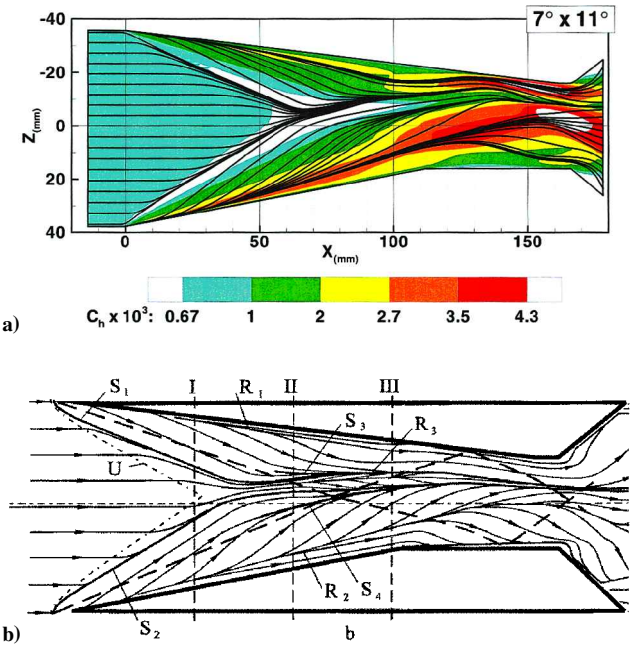

Fig. 5 The 7 × 11 deg a) skin-friction lines and heat-transfer coefficient on the bottom plate (Wilcox model) and b) topological scheme derived from the oil-flow visualization (from Ref. 15).

the primary shocks very close to the fins, plunge down to the bottom wall, go toward the centerline where they separate and are rolled up with SBL and VI. This is the entrainment flow (EF), constituted by high-energy fluid projected toward the bottom wall. The separation of EF yields two noticeable footprints on the bottom wall. On the 11-deg fin side the secondary convergence (or separation) line S_4 appears around $x = 70$ mm in the experiment (Fig. 5); a very similar line is present in the computation, although it appears significantly further downstream, around $x = 90$ mm. On the 7-deg fin side the origin of the experimental secondary convergence line S_3 is hardly distinguishable because this line seems to merge very fast with the primary separation line S_1; in the computation S_3 is in the exact extension of S_1, so that its origin cannot be clearly identified. However, the three-dimensional representation confirms that the $S_1 - S_3$ computed line corresponds to two different regimes of the flow.

In Fig. 4 a subregime to EF is identified (4s in green); these streamlines behave essentially the same way as EF until impinging the bottom wall, but then orient toward the fin rather than the centerline; consequently they are named the side entrainment flow (SEF). This subregime is not highlighted in Refs. 8, 9, and 17. The footprint of the boundary between EF and SEF is clearly visible in Fig. 5 as the two primary divergence lines close to the side walls (R_1 and R_2 in the topological scheme). It is clear that the highest heat transfers occur beneath EF, reaching a maximum exactly at the attachment lines. This is also true for the skin-friction coefficient, not displayed here. The last regime (Fig. 4, regime 3 in yellow) is the centerline vortex (CV). These lines originate from a region very close to the 11-deg fin, roughly at the middle height of the incoming boundary layer; after crossing the shock wave emanating from this fin, they plunge down to the bottom wall, go toward the centerline, and form a vortical flow underneath the space left free by the separation of left (cyan) and right (blue) EFs. Near the centerline this part of the flow encounters the attached boundary layer; both flows penetrate deeply streamwise and are associated with heat-transfer (and skin-friction) coefficients significantly lower than underneath EF (Fig. 5). The footprint of the attachment of CV to the bottom plate is the secondary attachment line R_3; it originates from between S_1 and S_2 in the experiment (Fig. 5), but from the 11-deg fin side in the computations (as just described).

Looking back at Fig. 3b, the observed rise of the computed heat-transfer coefficient along the TML can now be understood: it begins when the EF reaches the TML ($x \simeq 90$ mm), and the first maximum occurs when the attachment line R_2 crosses the TML ($x \simeq 135$ mm). The second maximum is also clearly linked to the same attachment line, crossing the TML again after having been deviated by the flow coming from the 7-deg fin side (Fig. 5).

Link with TKE

With the thermal model used, the heat-transfer coefficient is closely related to the skin-friction coefficient. The latter is proportional to the total shear stress, which is approximately reduced to its turbulent part in the logarithmic layer. Because the turbulent shear stress is roughly proportional to the TKE, high levels of skin friction and heat transfer are usually associated with high levels of TKE.

The regions of high levels of heat flux and skin friction have been found to correspond to the attachment lines of the three-dimensional flow originating from the upper part of the incoming boundary layer or even the inviscid part of the flow. This flow crosses the primary shock waves before plunging down to the bottom wall. One hypothesis put forward in the literature[12] is that two-equation turbulence models predict a too large increase in TKE in the outer part of the boundary layer across the shock waves, and that this excessive TKE is convected down to the wall because of the strong vortices formed behind the shocks. The following section is aimed at investigating one possible source of excessive TKE production through shock waves.

Realizability Corrections

Realizability Principles

The weak realizability principles[30,31] require the variances of the fluctuating velocity components to be positive and the cross correlations bounded by the Schwartz inequality:

$$\widetilde{u^2} \geq 0, \qquad \widetilde{v^2} \geq 0, \qquad \widetilde{w^2} \geq 0$$

$$\widetilde{uv}^2 \leq \widetilde{u^2}\widetilde{v^2}, \qquad \widetilde{uw}^2 \leq \widetilde{u^2}\widetilde{w^2}, \qquad \widetilde{vw}^2 \leq \widetilde{v^2}\widetilde{w^2} \tag{3}$$

Strictly speaking, these relations hold for statistical averages; with mass averaging the density fluctuations should be taken into account. Nevertheless, their effects are expected to be negligible. Any linear model based on the Boussinesq assumption can violate the constraints (3) in numerous circumstances, especially in the presence of strong pressure gradients. In such a model indeed, the turbulent stresses are linear with the traceless strain rate S°_{ij}:

$$\widetilde{u_i u_j}/k = -2(\nu_t/k)S^\circ_{ij} + \tfrac{2}{3}\delta_{ij} \tag{4}$$

and the turbulent viscosity ν_t is related to the TKE k and, somehow or other, to its specific dissipation $\omega = \epsilon/k$ by $\nu_t = c_\mu k/\omega$. The structural parameter $\widetilde{uv}/k$ is known to be constant in a large part of the boundary layer and to depend weakly on the pressure gradient. The constant value $c_\mu = 0.09$ is usually chosen to reproduce this behavior in the logarithmic region with no pressure gradient. Durbin indicates that, with such a model and for an incompressible flow, the realizability constraints are respected under the following conditions.[32]

Two-dimensional:

$$c_\mu s \leq \tfrac{2}{3} \Leftrightarrow \text{realizability (3)} \tag{5}$$

Three-dimensional:

$$c_\mu s \leq \tfrac{1}{\sqrt{3}} \Rightarrow \text{realizability (3)} \tag{6}$$

where s is the dimensionless strain invariant S/ω, with $S = \sqrt{(2S^\circ_{ij}S^\circ_{ij})}$. These conditions are obviously violated in the presence of strong velocity gradients. Because the TKE production rate is

$$P_k/\rho\epsilon = c_\mu s^2 - \tfrac{2}{3}S_{kk}\big/\omega \tag{7}$$

the infringement of a realizability constraint is a source of an important and nonphysical increase in TKE. Because SWBLI flows have numerous zones with strong velocity gradients and because the numerical solutions are suspected to contain zones where the TKE production is too strong, one should wonder whether these solutions are realizable.

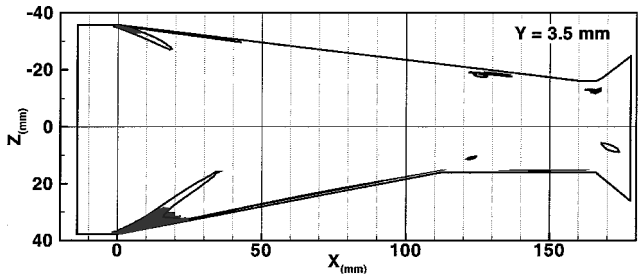

a) 7 × 11 deg

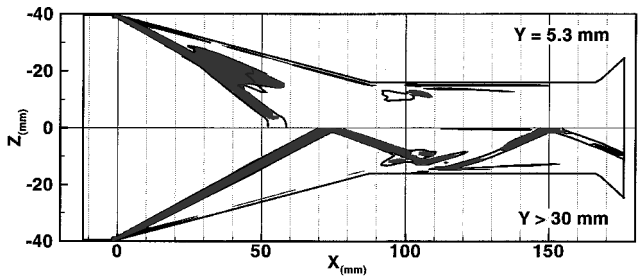

b) 15 × 15 deg

Fig. 6 Violation of realizability with the Wilcox model. Gray zones indicate the regions where the realizability constraints (3) are violated. Circled zones indicate the regions where $c_\theta s \geq 1/\sqrt{3}$.

Irrealizability of the Solutions

In the region of the flow located below the incoming boundary layer thickness δ_0, the constraints (3) are respected all over the bottom plate in each of the fine-grid solutions computed with the basic Wilcox's k–ω model (WI). However, some "irrealizable" zones appear above δ_0. The following description should remain true with virtually any usual two-equation turbulence model. In the 7 × 11 deg configuration, in the section $y = \delta_0$, the realizability constraints are violated within the foot of the primary shock waves (Fig. 6a); the irrealizable zone is larger on the 11-deg fin side than on the 7-deg fin side. Another irrealizable zone is very narrow and extends parallel to the fin, not far from the location of the primary attachment line. In the 15 × 15 deg configuration the irrealizable zone is even larger and occupies the whole upper part of the lambda foot of the primary shock waves (Fig. 6b, top). In the region of the flow not influenced by the bottom-wall boundary layer (above $y = 30$ mm, i.e., $8.5\delta_0$), the realizability constraints are violated across the shock waves only (Fig. 6b, bottom part), with certainly no significant impact on the flow in the vicinity of the bottom wall. In the weak interaction case (7 × 7 deg, not displayed here) no significant irrealizable zone is evidenced outside the vicinity of the inviscid shock waves. In Fig. 6 the regions where $c_\mu s > 1/\sqrt{3}$ are circled with thick solid lines. Relation (6) indicates that, in an incompressible flow, these circled regions should contain the irrealizable zones. It can be seen that, even in a compressible flow, the correlation between the $1/\sqrt{3}$ limit for $c_\mu s$ and irrealizability is very good. It confirms that $c_\mu s$ is a relevant parameter to control the extent of irrealizable zones.

Realizable Two-Equation Models

Several authors have considered the introduction of realizability constraints in two-equation Boussinesq turbulence models. The general idea is based on the observation that, through Eq. (4), the realizability can be ensured by decreasing properly the turbulent viscosity ν_t. In a recent review[33] Moore and Moore indicate that the correction can be written as a limitation of the constant in the constitutive relation:

$$\mu_t = \alpha_v c_\mu \rho(k/\omega) \qquad \text{with} \qquad \alpha_v = \min\{1, \bar{\alpha}_v\} \tag{8}$$

$$1/(\bar{\alpha}_v c_\mu) = A_0 + A_s\left(s^2 + A_r \varpi^2\right)^{\frac{1}{2}} \tag{9}$$

where ϖ is the dimensionless vorticity invariant Ω/ω, with $\Omega = \sqrt{(2\Omega_{ij}\Omega_{ij})}$. Moore and Moore propose a set of coefficients derived from an algebraic Reynolds-stress model ($A_0 = 2.85$, $A_s = 1.77$) and assuming, in a first approximation, that the strain

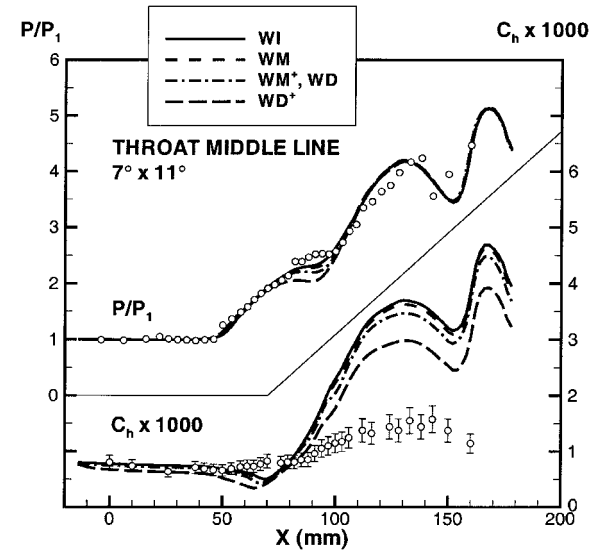

Fig. 7 7 × 11 deg. Medium grid. Pressure and heat-transfer coefficient on the bottom wall along the TML.

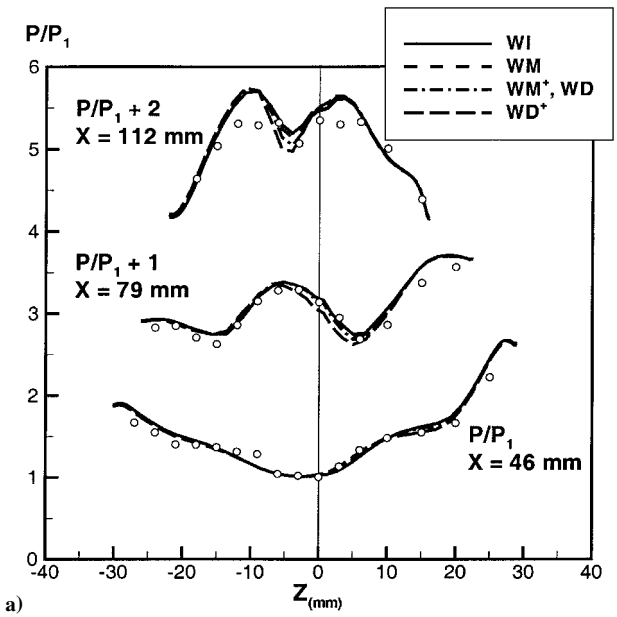

a)

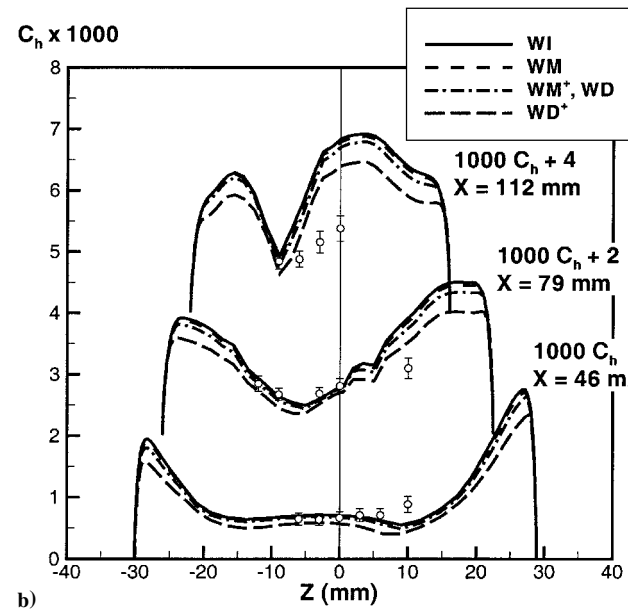

b)

Fig. 8 7 × 11 deg. Medium grid: a) pressure and b) heat-transfer coefficient on the bottom wall along three cross sections.

rate and rotation have symmetrical effects ($A_r = 1$). They show that, in the case of flows near the leading edge of blunt bodies, where the inviscid strain field is very large ($s = 100 - 400$) the modification results in a much better prediction of the TKE level. This kind of correction has also been shown to contribute significantly to cure the stagnation point anomaly as encountered in impinging jets. For instance, Durbin proposes a correction of the form (9) with $A_0 = A_r = 0$ and $1/A_s = c/\sqrt{3}$, where $c \leq 1$ ensures the realizability,[32] whereas $c = \frac{1}{2}$ is needed to get good results in the jet impingement problem.[34] With this last value the Durbin's proposal $1/A_s = 0.29$ leads to values of α_v significantly smaller than the Moore and Moore's expression and is virtually identical to the one by Menter[35] in the shear stress transport (SST) model, or by Coakley,[36,37] where $1/A_s = \sqrt{c_\mu} = 0.3$. [Actually, the expression proposed by Menter is not of the general form (8) and (9); it would match it if, when going from two to three dimensions, Menter had substituted $\sqrt{(S^2 + \Omega^2)}$ to $\partial U/\partial y$ instead of simply Ω. Only this point is missing to ensure that the SST model is realizable.[33]] In any case the turbulent transport equations are

$$D_t(\rho k) = P_k - \beta^\star \rho k \omega + \frac{\partial}{\partial x_J}\left[(\mu + \sigma^\star \mu_t)\frac{\partial k}{\partial x_J}\right] \quad (10)$$

$$D_t(\rho \omega) = \alpha \frac{\omega}{k}\left(\frac{P_{ki}}{\alpha_\omega} + P_{kc}\right) - \beta \rho \omega^2 + \frac{\partial}{\partial x_J}\left[(\mu + \sigma \mu_t)\frac{\partial \omega}{\partial x_J}\right] \quad (11)$$

where the constants are from the original model [except that, in the original model, $\omega = \epsilon/(c_\mu k)$, so that $\beta = \frac{3}{40}$ and $\beta^\star = c_\mu = 0.09$]: $\alpha = \frac{5}{9}$, $\beta = \frac{5}{6}$, $\beta^\star = 1$, $\sigma = \sigma^\star = \frac{1}{2}$. The TKE production rate is

$$P_k = P_{ki} + P_{kc} \quad \text{with} \quad P_{ki} = \mu_t S^2, \qquad P_{kc} = -\tfrac{2}{3}\rho k S_{kk} \quad (12)$$

The only question remaining is relative to the specific dissipation production rate: a first group of researchers[33,37] keeps the formal equation in its usual form ($\alpha_\omega = 1$), whereas the second group[29,32] recommends maintaining the incompressible part of the production term at its unmodified level by taking $\alpha_\omega = \alpha_v$. To determine the impact of the realizability enforcement on SWBLI, four models are tested: in the so-called Wilcox–Moore (WM) and Wilcox–Durbin (WD) models, α_ω is 1, and the realizability factor (8) and (9) is used to compute the eddy viscosity with the Moore and Moore[33] and Durbin[32] (with $c = \frac{1}{2}$) coefficients, respectively; the versions in which the production term in the specific dissipation equation is kept at its original and maximum level ($\alpha_\omega = \alpha_v$) are denoted WM$^+$ and WD$^+$, respectively.

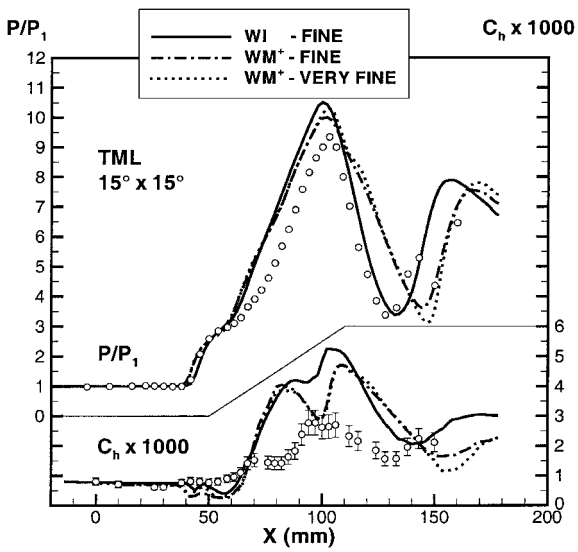

Fig. 9 15 × 15 deg. Pressure and heat-transfer coefficient on the bottom wall along the TML.

Effect of the Realizability Corrections

The solutions have been obtained in the three configurations, with the two different wall thermal conditions and on the coarse, medium, and fine grids with the WM$^+$ model. In the 15 × 15 deg configuration two additional computations were carried out with this model on the very fine grid. Additionally, the solutions have been obtained for the 7 × 11 deg configuration on the medium grid with the two different wall thermal conditions and all other models: WM, WD, WD$^+$. The conclusions drawn next rely on the whole set of computations, although only some of them are used for the illustration. In the 7 × 7 deg configuration, the pressure distribution is not influenced by the realizability corrections, and the skin-friction and heat-transfer coefficients are lowered by at most 5% in the interaction zone. It demonstrates that these corrections are not active in the case when the results are already quite good.

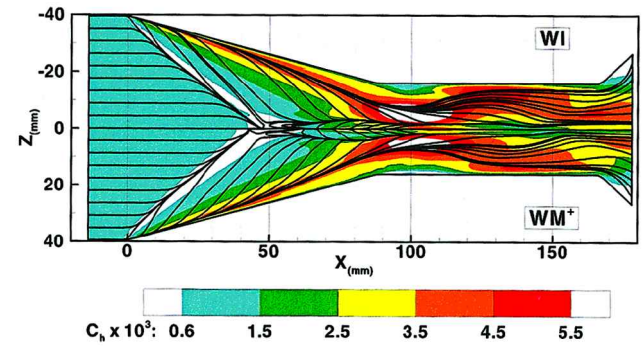

a) Numerical solutions on the bottom wall

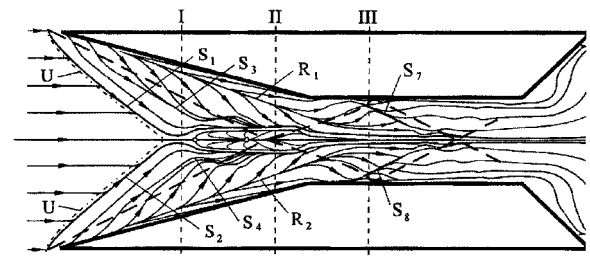

b) Experimental topological scheme on the bottom wall

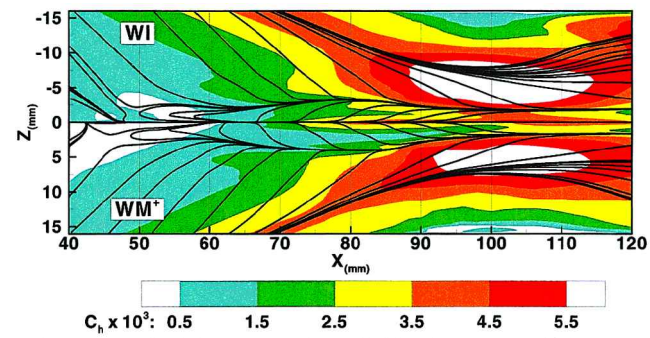

c) Numerical solutions in the central separation region

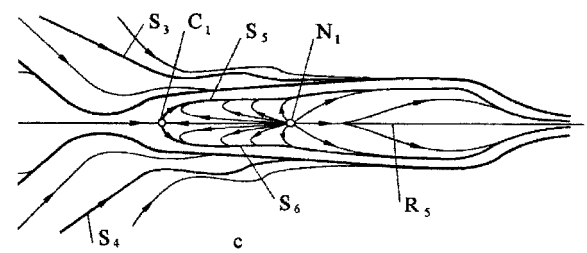

d) Experimental topological scheme in the central separation region

Fig. 10 15 × 15 deg. Computed skin-friction lines and heat-transfer coefficient (WI and WM$^+$ models) compared to the topological schemes derived from the oil-flow visualization (from Ref. 14) on the bottom wall.

Full Parametric Study in the 7 × 11 deg Configuration

In the 7 × 11 deg configuration the full parametric study is presented on the medium grid. The results obtained with the WI (Fig. 3b) and WM$^+$ (not displayed) models on both the medium and fine grids show that the difference in the heat-transfer coefficient caused by the grid is between 5–10% on the bottom wall. This accuracy is more than sufficient to ensure that at least the correct trends are captured on the medium grid. The pressure distribution is essentially unchanged by the realizability corrections (Fig. 7). The only noticeable difference occurs at the pressure plateau, visible on the TML between $x = 85 - 100$ mm, which corresponds to the formation of the secondary separation line S_4 (Fig. 5). This plateau, as evidenced by the measurements, is only a slight change in slope with the Wilcox's model, but a clearly apparent plateau with WM$^+$, WD, and WD$^+$, the level of which is nevertheless significantly underpredicted. In the cross sections no major difference appears between the models, which can reproduce fairly well the evolution of the pressure on the bottom wall, except at some particular locations (Fig. 8a): in the first cross section the importance of the pressure plateau underneath the incipient vortices (the EF) is slightly underestimated by the simulations; at the last cross section, the pressure is notably overestimated at the locations shown to be under the 7-deg fin side secondary separation line S_3 ($z \sim -10$ mm) and under the 11-deg fin side primary attachment line R_2 ($z \sim +10$ mm) in Fig. 5. None of the correction is able to improve the solution at these locations.

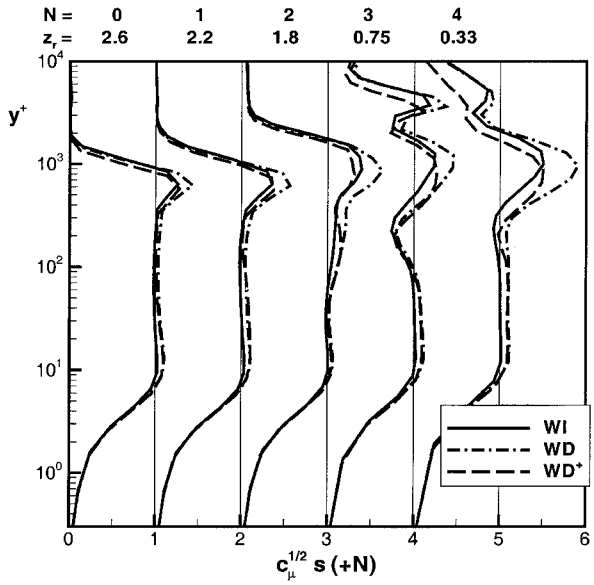

Fig. 11 7 × 11 deg. Medium grid. Profiles of the dimensionless strain rate invariant s in the cross section $x = 46$ mm.

The first peak of the heat-transfer coefficient along the TML (Fig. 7) is lowered by only 2 and 6% when using respectively the Moore and Moore (WM) and Durbin (WD) realizability factors in the definition of μ_t. The decrease goes to 6 and 20% when suppressing the indirect effect of the realizability factor on the specific dissipation production rate (WM$^+$ and WD$^+$, respectively). This decrease corresponds to a global trend as shown in the cross sections (Fig. 8b) but is obviously not sufficient to fill the gap between the computations and the measurements. Even though lowered by about 20% with the WD$^+$ model, the heat transfer underneath the main vortices (EF) is still high above the sparse experimental data available off the TML. In Figs. 7 and 8, the WM$^+$ and WD solutions are not distinguished because they are actually comparable to each other. This indicates that the same global effect is achieved by either lowering the realizability factor (going from WM to WD) or by suppressing its indirect effect on the specific dissipation production rate (when going from WM to WM$^+$). The global sketch of the skin-friction lines is essentially unmodified by the realizability corrections. A close comparison of the WI (Fig. 5) and WM$^+$ (not displayed) fine-grid solutions only shows that the secondary attachment line R_3 going between the two secondary separation lines S_3 and S_4 (and corresponding to the attachment of the CV) is significantly sharpened with the realizability correction.

Additional Information from the 15 × 15 deg Configuration

In the 15 × 15 deg configuration the WI and WM$^+$ fine-grid and the WM$^+$ very-fine-grid solutions are computed and compared in Fig. 9. The WM$^+$ solutions on both grids exhibit insignificant differences along the TML up to $x = 150$ mm. This confirms that the fine-grid solution is representative of the mesh-converged solution

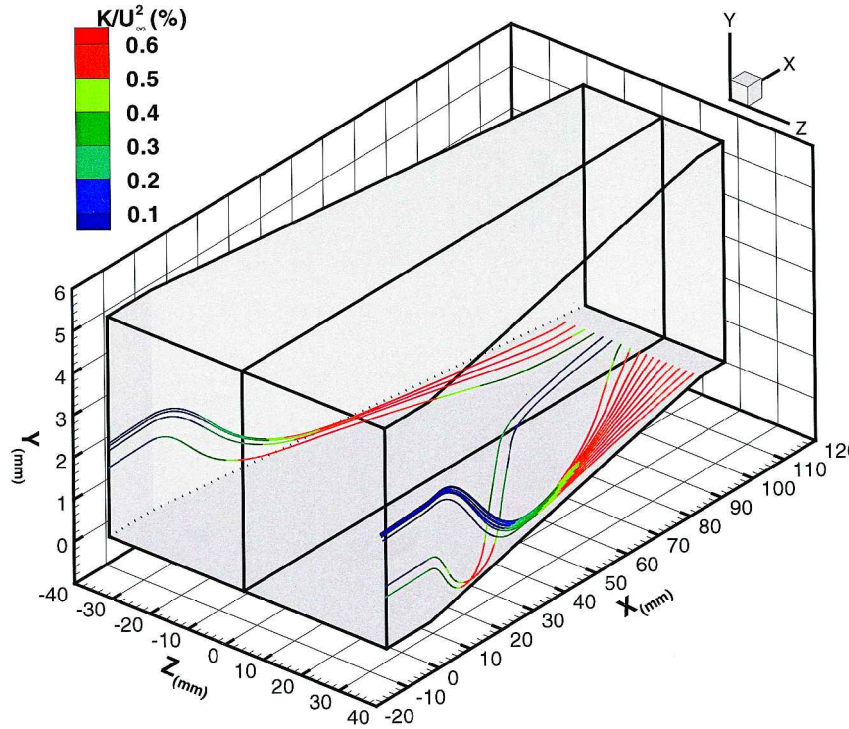

Fig. 12 7 × 11 deg. Wilcox model. Streamlines arriving 23 θ m above the bottom plate ($y^+ \sim 25$) in the cross section $x = 112$ mm and colored with the TKE level.

as already claimed. Differences up to 5–7% still persist in the peak value of the heat-transfer coefficient along the primary attachment line (not displayed) between the fine-grid and the very-fine-grid WM^+ solutions, which shows that this configuration demands really large ressources to be accurately computed (four million cells in half the configuration).

The realizability correction induces significant changes in the pressure distribution (Fig. 9). The maximum of pressure along the TML, occuring at the beginning of the influence of the expansion waves coming from the inner corner of the fins, is closer to the experimental data with the Moore and Moore correction. The pressure distribution along the first two cross sections, especially underneath EF, is globally improved by the realizability correction (not displayed). However, the gentler pressure slope at the level of the recirculation zone ($x = 50 - 65$ mm on the TML) is not well reproduced by any computation. Downstream of the pressure maximum, the pressure is worsened by the Moore and Moore correction.

The evolution of the Stanton number along the TML (Fig. 9) is closely related to the topology of the flow in the central separation region, which needs to be described in some more details (see Ref. 28 for a comprehensive description). First, the convergence lines S_1 and S_2 (Figs. 10a and 10b) form the symmetrical footprint of the incoming boundary-layer separation. In the experiment (Fig. 10b) a fluidic throat does exist between S_1 and S_2 (as in weaker interactions; see Fig. 5), and a central separation region is formed behind the saddle point C_1 (at $x = 50 - 51$ mm), bounded by the separation lines S_5, S_6 (Fig. 10d). This region is occupied by the CV. The Stanton number rises gently along the TML up to the node point N_1 ($x = 68 - 69$ mm). At this point the CV begins to reattach along the line R_5 (Fig. 10d). The measured heat-transfer coefficient first remains constant and then increases up to $x = 100$ mm where it reaches its maximum. It corresponds to the location where the central separation region begins to narrow under the influence of the expansion waves (Figs. 10b and 10d).

In the computations the topology in the central region is quite different, yielding significant differences in the secondary features, like the Stanton number. The primary separation lines S_1 and S_2 intersect at the point C_1, which is a node (and not a saddle point) at $x = 47 - 48$ mm (Figs. 10a and 10c). The separation lines S_5, S_6, which bound the central separation region, appear much closer to the TML than in the experiments. The Stanton number drops by a factor of two between C_1 and N_1, located at $x = 66 - 67$ mm. Afterward, the Stanton number goes on increasing, reaching a first maximum around $x = 85$ mm and a second one, even higher, around $x = 105$ mm (Fig. 9). These locations correspond, respectively, to the regions where the central separation region is the widest and the narrowest in the computations (Figs. 10a and 10c). Between both, in the region where the CV develops, the WI solution exhibits a plateau. In the WM^+ solution the plateau becomes a significant drop essentially because the central separation region is wider (Fig. 10c), which allows the vorticity of the CV to spread over a larger area. The realizability correction does not modify the computed topology so that the features of the Stanton number remain the same. Nevertheless, the levels are significantly modified, essentially because of the lower turbulence levels in the WM^+ solution, which allow a sooner appearance (i.e., farther from the TML) of the separation lines S_5, S_6 than in the WI solution, yielding a wider central separation region and a lower Stanton number between the maxima.

Failure of Usual Corrections for High-Speed Flows

Corrections Based on the Strain Rate/Vorticity Invariants

In the preceding section representative realizability corrections have been assessed. One of them has been shown to improve significantly the prediction of the heat transfer, but not sufficiently. It could be argued that by strengthening the realizability factor even better results could be achieved. To determine whether further improvement is possible with a correction based on the strain rate or vorticity invariant (s or ϖ), Fig. 11 is drawn. It represents the profiles of $s\sqrt{c_\mu}$ at different stations along the cross section $x = 46$ mm of the 11-deg fin side of the 7×11 deg configuration. This quantity is supposed to be one in the logarithmic layer of an incompressible boundary layer. The transverse reduced location z_r, indicated in Fig. 11 for each station, is zero at the fin and one at the location of the inviscid shock generated by the 11-deg fin. The stations are chosen to cover the entire region underneath the EF, where the heat transfer is maximum on the bottom plate. Figure 11 demonstrates that the asymptotic limit of s is respected in a large part of the logarithmic layer and that it is exceeded in the upper part because of the interaction with the shock wave (mainly its rear leg, close to the fin). The largest values of s at $x = 46$ mm remain below the realizability limit at $x = 46$ mm and do not exceed 10 in the whole 7×11 deg configuration. These values are at least one order of magnitude less than in the stagnation-point cases for which the realizability corrections have been shown to be highly beneficial.[32,33] It indicates that the large TKE levels in SWBLI computed flows are not linked to very large values of s although it is in the stagnation-point cases. Here, the variations of s are surely not sufficient to expect a significant improvement using only a strenghtened correction based on this parameter.

To support and to extend this statement, Fig. 12 is drawn. It is relative to the fine-grid solution obtained in the 7×11 deg configuration with the Wilcox's model. In this graph the streamlines arriving at the height of 23 μm ($y^+ \sim 25$) above the bottom plate at the cross section $x = 112$ mm are displayed and colored with the TKE level. It appears that, in the cross section $x = 112$ mm, the level of energy is quite high. As already described, the Stanton number and TKE high levels are intimately related to each other. The plot confirms that the highest levels of C_h are associated with the highest levels of TKE visible in the flow near the bottom plate. As already mentioned, one hypothesis is that two-equation turbulence models predict a too large increase in TKE in the outer part of the boundary layer across the shock waves and that this excessive TKE is convected down to the wall by the strong vortices formed behind the shocks. Figure 12 shows that the increase in TKE along the observed streamlines occurs rather when the EF approaches the bottom wall than when the streamlines cross the primary shock wave, near the fin leading edge. The corrections based on s or ϖ are active in the latter regions, but not in the former.

Turbulent Length-Scale Limit

In hypersonic flows Coakley and Huang[37] propose to limit the turbulent length scale ℓ to its value in the logarithmic part of an incompressible boundary layer:

$$\mu_t = \rho c_\mu k^{\frac{1}{2}} \ell \quad \text{with} \quad \ell = \min\left\{\ell_{\log}, \left(k^{\frac{1}{2}}/\omega\right)\right\}$$

$$\ell_{\log} = \left(\kappa / c_\mu^{\frac{3}{4}}\right) d \tag{13}$$

where d is the distance to the wall and κ is the von Kármán constant ($\kappa / c_\mu^{3/4} = 2.5$); then the value of the dissipation term in the TKE transport equation is recomputed according to $\omega = k^{1/2}/\ell$. To determine whether this correction could help in the SWBLI cases considered here, the ratio of the computed turbulent length scale $\ell = \alpha_v k^{1/2} \omega$ to the logarithmic expression $\ell_{\log}$ is examined in the solutions obtained with the different models. Figure 13 shows that this limit is violated indeed in the WI solution, but only slightly and in the upper part of the logarithmic layer. The realizability corrections tend to reduce the region where this limit is violated; in particular, the WD^+ model gives a solution where the turbulent length-scale limit is respected almost everywhere. Again, nearly the same effect is obtained by lowering the realizability factor (from WM to WD) or by avoiding the reduction of the specific dissipation production rate (from WM to WM^+). It can be concluded that the turbulent length-scale limit would not be of great help in this case and that a similar effect may be achieved in a more natural way by applying a realizability correction.

Compressibility Corrections

The primary manifestation of compressible turbulence is the appeareance of the dilatation dissipation in the TKE and dissipation equations. This occurs at high turbulent Mach numbers $M_t = \sqrt{(2k)}/a$, where a is the local speed of sound. The most popular

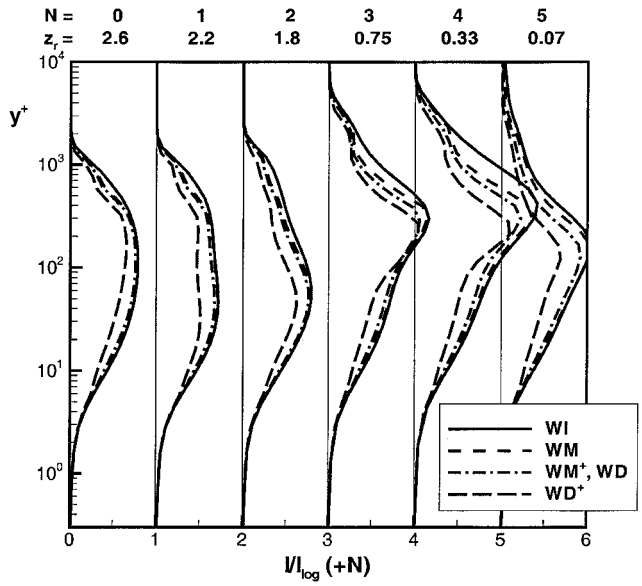

Fig. 13 7 × 11 deg. Medium grid. Profiles of the ratio of the turbulent length scale $\ell = \alpha_\nu k^{1/2}/\omega$ to its value in the logarithmic layer (2.5y) in the cross section $x = 46$ mm.

corrections have been primarily derived for compressible mixing layers by Sarkar et al.[38] and Zeman.[39] However, they have been shown to lead to undesirably lowered skin-friction coefficients in turbulent boundary layers.[26,37,40] In the wall regions the so-called compressibility corrections should not be active at least when the turbulent Mach number is under the threshold $M_{to} = 0.25$ (Ref. 26). The maximum turbulent Mach number in the WI solution is 0.3. For this value the increase of the dissipation term is only 4% according to the Wilcox's compressibility correction.[26] The WM$^+$, WD, and WD$^+$ solutions give values of M_t below the compressible threshold all over the computational domain. It can be concluded that this kind of correction would be of no help in the considered cases.

Conclusions

Weak and strong, symmetrical and asymmetrical crossing-shock-wave/boundary-layer interactions have been analyzed on the basis of both experiments and computations. The computations were carried out on meshes up to four million cells, by solving the Reynolds-averaged Navier–Stokes equations with Wilcox's k–ω model. Mesh-converged solutions are achieved in each case. It is demonstrated that inadequately refined grids can yield deceptively close agreement with experimental heat transfer, thereby emphasizing the need for a detailed grid-refinement study in each configuration. The refined analysis of the structure of the flow shows that the overprediction of heat transfer is clearly linked to the attachment to the bottom wall of the vortices forming downstream of the primary shock waves. It is demonstrated that the stronger the interaction, the more the numerical solutions violate the realizability principles, essentially in the upper part of the bottom-plate boundary layer and accross the shock waves. By introducing a dependence of c_μ on the velocity gradients, realizable solutions are obtained. The heat-transfer coefficients are effectively lowered, as much as by 20% with the Durbin[32] correction, which is nevertheless insufficient to meet the experimental data. No further improvement can be expected either from corrections based on the strain rate invariant, or from the turbulent length-scale limit for hypersonic flows,[37] or yet from any usual compressibility correction.[26,38,39] The streamlines arriving near the wall in the regions of overpredicted heat-transfer coefficients are shown to originate from the very narrow regions close to the fin leading edges, in the upper part of the incoming boundary layer, and to be associated with an increase of turbulent kinetic energy when approaching the bottom wall, rather than when crossing the shock waves. This problem, specific to the interaction of a swept shock wave with a fully developed turbulent boundary layer, needs to receive special attention from the turbulence modeling community.

Acknowledgments

This work was done while the first author was a Visiting Research Scholar at Rutgers University, as a recipient of a research fellowship awarded by the French Délégation Générale pour l'Armement (DGA), Direction des Systèmes de forces et de la Prospective, under Grants ERE 981075 and 9960053. The work was supported in part by the Service des Programmes Aéronautiques of the DGA under Grant 90-95-005 BC-80. The authors affiliated with the Institute of Theoretical and Applied Mechanics were supported by the Russian Foundation of Basic Research (Grant 97-01-00885) and the U.S. Air Force European Office of Aerospace Research and Development (Contract F61708-97-W0136 monitored by C. Raffoul). The computational resources were provided by the National Science Foundation at the National Center for Supercomputing Applications, University of Illinois at Urbana–Champaign under Grant MSS990001N. Finally, the authors wish to thank Omar Besbes, graduating from École Polytechnique, France, for his help in performing some of the computations and B. Aupoix for his helpful comments on earlier versions of the manuscript.

References

[1] *Shock-Wave/Boundary-Layer Interactions in Supersonic and Hypersonic Flows*, R 792, AGARD, Aug. 1993.

[2] Settles, G. S., "Swept Shock/Boundary-Layer Interactions—Scaling Laws, Flowfield Structure, and Experimental Methods," *Shock-Wave/Boundary-Layer Interactions in Supersonic and Hypersonic Flows*, R 792, AGARD, Aug. 1993, pp. 1-1–1-40.

[3] Garrison, T. J., and Settles, G. S., "Flowfield Visualization of Crossing Shock-Wave/Boundary-Layer Interactions," AIAA Paper 92-0750, Jan. 1992.

[4] Garrison, T. J., and Settles, G. S., "Interaction Strength and Model Geometry Effects on the Structure of Crossing-Shock Wave/Turbulent Boundary-Layer Interactions," AIAA Paper 93-0780, Jan. 1993.

[5] Garrison, T. J., Settles, G. S., Narayanswami, N., and Knight, D. D., "Structure of Crossing-Shock-Wave/Turbulent-Boundary-Layer Interactions," *AIAA Journal*, Vol. 31, No. 12, 1993, pp. 2204–2211.

[6] Garrison, T. J., Settles, G. S., Narayanswami, N., and Knight, D. D., "Laser Interferometer Skin-Friction Measurements of Crossing-Shock-Wave/Turbulent-Boundary-Layer Interactions," *AIAA Journal*, Vol. 32, No. 6, 1994, pp. 1234–1241.

[7] Garrison, T. J., Settles, G. S., Narayanswami, N., Knight, D. D., and Horstman, C. C., "Flowfield Surveys and Computations of a Crossing-Shock Wave/Boundary-Layer Interaction," *AIAA Journal*, Vol. 34, No. 1, 1996, pp. 50–56.

[8] Gaitonde, D., Shang, J. S., and Visbal, M., "Structure of a Double-Fin Turbulent Interaction at High Speed," *AIAA Journal*, Vol. 33, No. 2, 1995, pp. 193–200.

[9] Gaitonde, D., and Shang, J. S., "Structure of a Turbulent Double-Fin Interaction at Mach 4," *AIAA Journal*, Vol. 33, No. 12, 1995, pp. 2250–2258.

[10] Knight, D. D., "Numerical Simulation of 3-D Shock Wave Turbulent Boundary Layer Interactions," *Shock-Wave/Boundary-Layer Interactions in Supersonic and Hypersonic Flows*, R 792, AGARD, Aug. 1993, pp. 3-1–3-32.

[11] Knight, D. D., and Degrez, G., "Shock Wave Boundary Layer Interactions in High Mach Number Flows—A Critical Survey of Current CFD Prediction Capabilities," *Hypersonic Experimental and Computational Capability, Improvement and Validation*, edited by J. Muylaert, A. Kumar, and C. Dujahric, AR 319, Vol. 2, AGARD, Dec. 1998, pp. 1-1–1-35.

[12] Knight, D. D., "Simulation of Shock Wave-Turbulent Boundary Layer Interactions Using the Reynolds-Averaged Navier–Stokes Equations," *Modeling Complex Turbulent Flows*, edited by M. D. Salas, J. N. Hefner, and L. Sakell, *ICASE/LaRC Interdisciplinary Series in Science and Engineering*, Vol. 7, Kluwer, Norwell, MA, 1999, pp. 277–296.

[13] Zheltovodov, A. A., Maksimov, A. I., Shevchenko, A. M., Vorontsov, S. S., and Knight, D. D., "Experimental Study and Computational Comparison of Crossing Shock Wave/Turbulent Boundary Layer Interaction," *International Conference on the Methods of Aerophysical Research*, Pt. I, Inst. of Theoretical and Applied Mechanics, Siberian Branch of the Russian Academy of Sciences, Novosibirsk, Russia, 1994, pp. 221–230.

[14] Zheltovodov, A. A., Maksimov, A. I., and Shevchenko, A. M., "Topology of Three-Dimensional Separation Under the Conditions of Symmetric Interaction of Crossing Shocks and Expansion Waves with Turbulent Boundary Layer," *Thermophysics and Aeromechanics*, Vol. 5, No. 3, 1998, pp. 293–312.

[15] Zheltovodov, A. A., Maksimov, A. I., Shevchenko, A. M., and Knight, D. D., "Topology of Three-Dimensional Separation Under the Conditions of Asymmetrical Interaction of Crossing Shocks and Expansion Waves with

Turbulent Boundary Layer," *Thermophysics and Aeromechanics*, Vol. 5, No. 4, 1998, pp. 483–503.

[16]Knight, D. D., Garrison, T. J., Settles, G. S., Zheltovodov, A. A., Maksimov, A. I., Shevchenko, A. M., and Vorontsov, S. S., "Asymmetric Crossing-Shock-Wave/Turbulent-Boundary-Layer Interaction," *AIAA Journal*, Vol. 33, No. 12, 1995, pp. 2241–2249.

[17]Gaitonde, D. V., Shang, J. S., Garrison, T. J., Zheltovodov, A. A., and Maksimov, A. I., "Three-Dimensional Turbulent Interactions Caused by Asymmetric Crossing-Shock Configurations," *AIAA Journal*, Vol. 37, No. 12, 1999, pp. 1602–1608.

[18]Panaras, A. G., "Algebraic Turbulence Modeling for Swept Shock-Wave/Turbulent Boundary-Layer Interactions," *AIAA Journal*, Vol. 35, No. 3, 1997, pp. 456–463.

[19]Panaras, A. G., "The Effect of the Structure of Swept Shock-Wave/Turbulent Boundary-Layer Interactions on Turbulence Modelling," *Journal of Fluid Mechanics*, Vol. 338, May 1997, pp. 203–230.

[20]Baldwin, B. S., and Lomax, H., "Thin Layer Approximation and Algebraic Model for Separated Turbulent Flows," AIAA Paper 78-257, Jan. 1978.

[21]Gaitonde, D. V., Visbal, M. R., Shang, J. S., Zheltovodov, A. A., and Maksimov, A. I., "Parametric Investigation of Flowfield Structure and Validation Issues in 3-D Crossing-Shock Wave/Turbulent Boundary Layer Interactions," *International Conference on the Methods of Aerophysical Research*, Pt. I, Inst. of Theoretical and Applied Mechanics, Siberian Branch of the Russian Academy of Sciences, Novosibirsk, Russia, 1998, pp. 67–76.

[22]Lokotko, A. V., and Shushpanov, M. M., "Thermal Wind Tunnel T-333," *Aerophysical Research*, USSR Academy of Sciences, Siberian Div., 1972, pp. 18–20 (in Russian).

[23]Zaikovsky, V. N., Zaulichny, E. G., Melamed, B. M., and Senov, Y. M., "An Experimental Investigation of Local Heat-Exchange Coefficients on the Walls of a Valve Mechanism," *Journal of Applied Mechanics and Technical Physics*, Vol. 23, No. 2, 1982, pp. 205–210.

[24]"GASP, General Aerodynamic Simulation Program Version 3," User's Manual, AeroSoft, Inc., Blacksburg, Virginia, May 1996.

[25]Wilcox, D. C., "Reassessment of the Scale-Determining Equation for Advanced Turbulence Models," *AIAA Journal*, Vol. 26, No. 11, 1988, pp. 1299–1310.

[26]Wilcox, D. C., *Turbulence Modeling for CFD*, 2nd ed., DCW Industries, Inc., La Cañada, CA, 1998, pp. 175–177, 244–245.

[27]Thivet, F., Besbes, O., and Knight, D. D., "Effect of Grid Resolution on Accuracy of Skin Friction and Heat Transfer in Turbulent Boundary Layers," AIAA Paper 2000-0820, Jan. 2000.

[28]Thivet, F., Knight, D. D., Zheltovodov, A. A., and Maksimov, A. I., "Numerical Prediction of Heat Transfer in Supersonic Inlets," European Congress on Computational Methods in Applied Sciences and Engineering, ECCOMAS, Sept. 2000.

[29]Thivet, F., Knight, D. D., Zheltovodov, A. A., and Maksimov, A. I., "Some Insights in Turbulence Modeling for Crossing-Shock-Wave/Boundary-Layer Interactions," AIAA Paper 2000-0131, Jan. 2000.

[30]Schumann, U., "Realisability of Reynolds Stress Turbulence Models," *Physics of Fluids*, Vol. 20, No. 5, 1977, pp. 721–725.

[31]Lumley, J. L., "Computational Modeling of Turbulent Flows," *Advances in Applied Mechanics*, Vol. 18, Academic Press, New York, 1978, pp. 123–176.

[32]Durbin, P. A., "On the k–ϵ Stagnation Point Anomaly," *International Journal of Heat and Fluid Flow*, Vol. 17, No. 1, 1996, pp. 89, 90.

[33]Moore, J. G., and Moore, J., "Realizability in Two-Equation Turbulence Models," AIAA Paper 99-3779, June–July 1999.

[34]Behnia, M., Parneix, S., and Durbin, P. A., "Simulation of Jet Impingement Heat Transfer with the k–ϵ–v^2 Model," *Annual Research Briefs 1996*, CTR, Stanford, California, 1996, pp. 3–16 (http://ctr.stanford.edu/ResBriefs96/behnia.ps.Z).

[35]Menter, F. R., "Two-Equation Eddy-Viscosity Turbulence Models for Engineering Applications," *AIAA Journal*, Vol. 32, No. 8, 1994, pp. 1598–1605.

[36]Coakley, T. J., "Turbulence Modeling Methods for the Compressible Navier–Stokes Equations," AIAA Paper 83-1693, June 1983.

[37]Coakley, T. J., and Huang, P. G., "Turbulence Modeling for High Speed Flows," AIAA Paper 92-0436, Jan. 1992.

[38]Sarkar, S., Erlebacher, G., Hussaini, M. Y., and Kreiss, H. O., "The Analysis and Modelling of Dilatational Terms in Compressible Turbulence," *Journal of Fluid Mechanics*, Vol. 227, June 1991, pp. 473–493.

[39]Zeman, O., "Dilatation Dissipation: The Concept and Application in Modeling Compressible Mixing Layers," *Physics of Fluids*, Vol. 2, No. 2, 1990, pp. 178–188.

[40]Aupoix, B., Desmet, E., and Viala, S., "Hypersonic Turbulent Boundary Layer Modelling," *Transitional and Turbulent Compressible Flows*, edited by L. D. Kral and T. A. Zang, FED-Vol. 151, American Society of Mechanical Engineers, New York, 1993, pp. 175–182.

R. M. C. So
Associate Editor

Color reproductions courtesy of ONERA.